

# Continuation and stability of convective modulated rotating waves in spherical shells

F. Garcia, M. Net, and J. Sánchez  
*Dept. de Física Aplicada,  
Universitat Politècnica de Catalunya,  
Campus Nord, Mòdul B4,  
Jordi Girona Salgado 1-3, 08034 Barcelona, Spain*

(Dated: February 2, 2016)

Modulated rotating waves (MRW), bifurcated from the thermal-Rossby waves which arise at the onset of convection of a fluid contained in a rotating spherical shell, and their stability, are studied. For this purpose, Newton-Krylov continuation techniques are applied. Non-slip boundary conditions, an Ekman number  $E = 10^{-4}$ , and a low Prandtl number fluid  $\sigma = 0.1$  in a moderately thick shell of radius ratio  $\eta = 0.35$ , differentially heated, are considered. The MRW are obtained as periodic orbits by rewriting the equations of motion in the rotating frame of reference where the rotating waves become steady states. Newton-Krylov continuation allows to obtain unstable MRW that cannot be found by using only time integrations, and identify regions of multistability. For instance, unstable MRW without any azimuthal symmetry have been computed. It is shown how they become stable in a small Rayleigh-number interval, in which two branches of traveling waves are also stable. The study of the stability of the MRW helps to locate and classify the large sequence of bifurcations which takes place in the range analyzed. In particular, tertiary Hopf bifurcations giving rise to three-frequency stable solutions are accurately determined.

## I. INTRODUCTION

The study of thermal convection in rotating spherical geometries is important for understanding the dynamics of astrophysical and geophysical phenomena such as the transport of energy in the interior of planets and stars or the differential rotation observed in the atmospheres of the major planets. In addition, magnetic fields of cosmic bodies are generated by convection of electrically conducting fluids in their interiors. In the last decades, many experimental, theoretical and numerical studies (see for instance [3, 5, 17, 20, 23, 28]), devoted to improve the understanding of the basic mechanisms which govern the convection and dynamo action in spherical geometry, have appeared. Good reviews can be found in the literature, see for instance [16] and [26].

Most of the set-ups of laboratory experiments are not well suited for measurements of flows near the onset of convection at small  $E$  and  $\sigma$ , so it is difficult to find a description of periodic flows, observed experimentally, in this range of parameters. From the analytical point of view the nonlinear nature of the equations and the spherical geometry of the domain lead to mathematical issues of very difficult treatment. For this reason, the development and improvement of the numerical techniques is basic to go deeply into the study of weakly supercritical nonlinear flows.

In problems having  $\mathcal{SO}(2)$  symmetry, convection takes the form of waves traveling in the azimuthal direction (thermal Rossby waves for  $\sigma = 0.1$ ), i.e. of rotating waves (RW), when the axisymmetry of the basic conduction state is broken. A secondary Hopf bifurcation gives rise to MRW, which may have different types of spatio-temporal symmetries [14, 29]. In [14] several examples in which rotating waves can exist, such as the

Taylor-Couette system or the meandering spiral waves in the Belousov-Zhabotinsky reaction, among others, are described. In the case of rotating spheres, RW and MRW were studied mainly with the help of direct numerical simulations (see [1, 2, 6, 36, 37, 43], among many others). When the azimuthal symmetry of the equations is constrained, time integrations allow to obtain some unstable MRW and their bifurcation diagrams [11]. However, the only use of time integrations is not sufficient to provide a complete picture of the dynamics. Specifically, time integration methods are unable to obtain unstable oscillatory solutions when all the symmetries of the flow are broken. These solutions might be relevant in organizing the global dynamics [18]. To find them and provide a deeper description of the phase space, continuation methods [19, 25, 32, 34] must be used.

In the fluid dynamics context numerical bifurcation analysis has been successfully applied during the last years to a great variety of problems [4, 18, 40–42]. Computations based on continuation of periodic orbits of non-trivial time dependence [39] and even tori [33, 35] or other invariant objects [38] have provided useful information to clarify the dynamics. In the case of rotating spherical geometries the bifurcation diagrams and the stability of the RW in the slowly rotating regime, for  $\sigma = 1$ , were studied in [21] with non-slip boundary conditions by means of Newton's method. At lower  $E$  and  $\sigma$ , and for a radius ratio  $\eta = 0.35$  corresponding to the estimated Earth's outer core, Newton-Krylov continuation techniques and Arnoldi methods were applied successfully in [31] to explain the coexistence of stable RW due to the presence of a double-Hopf bifurcation, and to understand the existence of amplitude and shape MRW from the symmetry breaking of the eigenfunctions at the secondary bifurcations.

Aside from the use of non-slip boundary conditions and low  $\sigma = 0.1$  and  $E = 10^{-4}$  values, the main novelty of this study is to obtain branches of MRW bifurcated from the RW previously studied in [31], using continuation techniques and to perform a stability analysis of these waves to study bifurcations to more complex flows such as three-frequency waves. The MRW are obtained as periodic orbits by rewriting the equations of motion in the rotating frame of reference in which the RW are steady solutions.

The paper is organized as follows. In Sec. II we introduce the formulation of the problem, and briefly describe the numerical method used to obtain and integrate the discretized equations. In Sec. III preceding results concerning the calculation of the RW are summarized. In Sec. IV the equations for the MRW, and the continuation and stability analysis methods are explained. The bifurcation diagrams as a function of the Rayleigh number,  $Ra$ , and the patterns of convection are shown in Sec. V, focusing mainly on the results that cannot be studied with just time integrations. Finally, in Sec. VI the paper ends with a brief summary of the results obtained.

## II. THE MODEL AND THE EQUATIONS

We consider the thermal convection of a fluid filling the gap between two concentric spheres differentially heated, rotating about an axis of symmetry with constant angular velocity  $\boldsymbol{\Omega} = \Omega \mathbf{k}$ , and subject to radial gravity  $\mathbf{g} = -\gamma \mathbf{r}$ , where  $\gamma$  is constant and  $\mathbf{r}$  the position vector. The mass, momentum and energy equations are written in the rotating frame of reference. The units are  $d = r_o - r_i$  for the distance,  $\nu^2/\gamma\alpha d^4$  for the temperature, and  $d^2/\nu$  for the time. In the previous definitions  $r_i$  and  $r_o$  are the inner and outer radii, respectively,  $\nu$  the kinematic viscosity, and  $\alpha$  the thermal expansion coefficient.

We use the Boussinesq approximation and the solenoidal velocity field is expressed in terms of toroidal,  $\Psi$ , and poloidal,  $\Phi$ , potentials

$$\mathbf{v} = \nabla \times (\Psi \mathbf{r}) + \nabla \times \nabla \times (\Phi \mathbf{r}). \quad (1)$$

Consequently, the equations for both potentials, and the temperature perturbation,  $\Theta = T - T_c$ , from the conduction state  $\mathbf{v} = \mathbf{0}, T = T_c(r)$ , with  $r = |\mathbf{r}|$  and  $T_c(r) = T_0 + Ra \eta/\sigma(1 - \eta)^2 r$ , are

$$\begin{aligned} [(\partial_t - \nabla^2)L_2 - 2E^{-1}\partial_\varphi] \Psi &= -2E^{-1}\mathcal{Q}\Phi - \\ &- \mathbf{r} \cdot \nabla \times (\boldsymbol{\omega} \times \mathbf{v}), \end{aligned} \quad (2)$$

$$\begin{aligned} [(\partial_t - \nabla^2)L_2 - 2E^{-1}\partial_\varphi] \nabla^2\Phi + L_2\Theta &= 2E^{-1}\mathcal{Q}\Psi + \\ &+ \mathbf{r} \cdot \nabla \times \nabla \times (\boldsymbol{\omega} \times \mathbf{v}), \end{aligned} \quad (3)$$

$$\begin{aligned} (\sigma\partial_t - \nabla^2)\Theta - Ra\eta(1 - \eta)^{-2}r^{-3}L_2\Phi &= \\ &- \sigma(\mathbf{v} \cdot \nabla)\Theta, \end{aligned} \quad (4)$$

where  $\boldsymbol{\omega} = \nabla \times \mathbf{v}$  is the vorticity.

The parameters of the problem are the Rayleigh number  $Ra$ , the Prandtl number  $\sigma$ , the Ekman number  $E$ , and the radius ratio  $\eta$ . They are defined by

$$Ra = \frac{\gamma\alpha\Delta T d^4}{\kappa\nu}, \quad E = \frac{\nu}{\Omega d^2}, \quad \sigma = \frac{\nu}{\kappa}, \quad \eta = \frac{r_i}{r_o}, \quad (5)$$

where  $\kappa$  is the thermal diffusivity, and  $\Delta T > 0$  the difference in temperature between the inner and outer boundaries.

The operators  $L_2$  and  $\mathcal{Q}$  are defined by  $L_2 \equiv -r^2\nabla^2 + \partial_r(r^2\partial_r)$ ,  $\mathcal{Q} \equiv r \cos\theta\nabla^2 - (L_2 + r\partial_r)(\cos\theta\partial_r - r^{-1}\sin\theta\partial_\theta)$ ,  $(r, \theta, \varphi)$  being the spherical coordinates, with  $\theta$  measuring the colatitude, and  $\varphi$  the longitude. Non-slip perfect thermally conducting boundaries are used

$$\Phi = \partial_r\Phi = \Psi = \Theta = 0 \quad \text{at} \quad r = r_i, r_o. \quad (6)$$

The equations are discretized and integrated as described in [10] and references therein. The potentials and the temperature perturbation are expanded in spherical harmonics in the angular coordinates, truncated at degree  $L_{max}$ . In the radial direction a collocation method on a Gauss-Lobatto mesh of  $n_r + 1$  points is used. The code is parallelized in the spectral and physical spaces by using OpenMP directives (see [9]). We use optimized libraries (FFTW3 [7]) for the FFTs in  $\varphi$  and matrix-matrix products (DGEMM GOTO [15]) for the Legendre transforms in  $\theta$  when computing the nonlinear terms.

For the time integration high order implicit-explicit backward differentiation formulas (IMEX-BDF) [10] are used. In the IMEX method we treat the nonlinear terms explicitly in order to avoid solving nonlinear equations at each time step. The Coriolis term is treated fully implicitly to allow larger time steps. The use of matrix-free Krylov methods (GMRES in our case) for the linear systems facilitates the implementation of a suitable order and time step-size control.

## III. COMPUTATION AND STABILITY OF THE ROTATING WAVES

In this section some background necessary to follow easily Secs. IV and V is included.

The discretization of equations (2-4) leads to a system of  $n = (3L_{max}^2 + 6L_{max} + 1)(n_r - 1)$  ordinary differential equations (ODE) of the form

$$L_0\partial_t u = Lu + B(u, u), \quad (7)$$

where  $u = (\Psi_l^m(r_i), \Phi_l^m(r_i), \Theta_l^m(r_i))$  is the vector containing the values of the spherical harmonic coefficients at the inner radial collocation points, and  $L_0$  and  $L$  are linear operators which include the boundary conditions. The former is invertible. It is the identity acting on  $\Psi_l^m$  and  $\Theta_l^m$ , and the operator  $\mathcal{D}_l$  acting on  $\Phi_l^m$  (see [31] for details). The operator  $L$  includes all the linear terms and depends on the parameters of the problem, in particular

on the Rayleigh number  $Ra$ , that will be the control parameter of this study. The rest of parameters are fixed to  $\eta = 0.35$ ,  $E = 10^{-4}$  and  $\sigma = 0.1$ . Therefore,  $p = Ra$  and  $L = L(p)$ . The bilinear operator  $B$  only contains the non-linear (quadratic) terms.

The system is  $\mathcal{SO}(2) \times \mathcal{Z}_2$ -equivariant,  $\mathcal{SO}(2)$  generated by azimuthal rotations, and  $\mathcal{Z}_2$  by reflections with respect to the equatorial plane. According to bifurcation theory, the first bifurcation, which breaks the axisymmetry of the conductive state, is a Hopf bifurcation giving rise to RW. In the linear stability analysis of [12] and [31], critical values  $p = p_1$ , at which there are vectors  $v_c$  and precession frequencies  $\omega_c$  satisfying  $i\omega_c L_0 v_c = L v_c$ , were obtained as a function of  $E$  and  $\eta$ , respectively. With  $\sigma = 0.1$ ,  $\eta = 0.35$  and  $E = 10^{-4}$  the preferred eigenfunctions are symmetric with respect to the equator. The precession frequencies  $\omega_c$  are negative, namely the drifting velocities  $c = -\omega_c/m$  are positive, thus the waves travel in the prograde direction. Moreover, they consist in quasi-geostrophic convective columns attached to the inner sphere of mean radius  $r_c \ll d$ .

Rotating waves,  $u(r, \theta, \varphi - \omega t) = \tilde{u}(r, \theta, \tilde{\varphi})$ , with  $\tilde{\varphi} = \varphi - \omega t$ , were obtained in [31] by Newton-Krylov continuation methods as steady solutions of the system (omitting the tildes)

$$F(u, \omega, p) \equiv L(p)u + B(u, u) + \omega L_0 \partial_\varphi u = 0, \quad (8)$$

by using a suitable preconditioner to accelerate the convergence of the linear solver. Their stability was studied by considering a perturbation  $v(t, r, \theta, \tilde{\varphi})$  of  $u(r, \theta, \tilde{\varphi})$  and linearizing Eq. (8). The leading eigenvalues of the matrix  $L_0^{-1} D_u F(u)$  were computed using the ARPACK package [22], based on Arnoldi algorithms, and shift-invert strategies [24].

The bifurcation diagrams were calculated for the values of the parameters above mentioned, i.e. for  $E = 10^{-4}$ ,  $\sigma = 0.1$ , control parameter  $p = Ra$ , and different values of the radius ratio  $\eta$ , around the vicinity of a double-Hopf bifurcation.

Figures 1(a,b), taken from [31], show the  $\mathcal{L}_2$ -norm of the RW and the drifting frequency,  $\omega$ , respectively, versus  $Ra$  for  $\eta = 0.35$ . The horizontal axis in Fig. 1(a) corresponds to the basic conductive state  $\|u\|_2 = 0$ . In these figures, solid and dashed lines indicate stable and unstable solutions, respectively. The preferred mode at the onset of convection ( $Ra_c = 1.856 \times 10^5$ ), has a six-fold rotational symmetry. At the bifurcation point a branch of supercritical stable RW keeping this symmetry emerges. Other branches bifurcated from the conduction state at higher  $Ra$ , invariant under  $2\pi/m$  rotations ( $m = 5, 7, 8, 4, \dots$ ), are unstable. However that with the five-fold symmetry stabilizes after a Hopf bifurcation at  $Ra = 2.043428 \times 10^5$  which breaks the five-fold symmetry. An unstable branch of MRW without any azimuthal symmetry is born at this point. This behavior was related with the existence of a double-Hopf bifurcation at a slightly different value of  $\eta$  (0.3308), involving the modes of azimuthal wave numbers  $m = 5$  and  $m = 6$ . The

branches of five- or six-fold symmetric RW lose their stability via new Hopf bifurcations at  $Ra = 2.584388 \times 10^5$  and  $Ra = 2.738518 \times 10^5$ , giving rise to branches of stable MRW, which keep the symmetry of the RW.

#### IV. COMPUTATION AND STABILITY OF THE MODULATED ROTATING WAVES

As said before, the RW undergo secondary Hopf bifurcations at critical values  $p$ , giving rise to branches of MRW. These are solutions for which there exist a minimal time  $\tau > 0$  and a rotating frequency  $\omega$  such that

$$u(\tau + t, r, \theta, \varphi) = u(t, r, \theta, \varphi - \omega\tau) \quad \forall t. \quad (9)$$

The time  $\tau$  is the period of the modulation in the frame of reference at which only the oscillations due to the modulation are observed, and  $\omega$  is the angular velocity of this frame of reference (relative to the rotating spheres).

Let us define  $u(t, r, \theta, \varphi) = \tilde{u}(t, r, \theta, \tilde{\varphi})$ , with  $\tilde{\varphi} = \varphi - \omega t$  and  $\omega$  a rotating frequency. If  $\tilde{u}$  is a  $\tau$ -periodic function, then  $u$  is a MRW because

$$\begin{aligned} u(t + \tau, r, \theta, \varphi) &\stackrel{1}{=} \tilde{u}(t + \tau, r, \theta, \varphi - \omega(t + \tau)) \stackrel{2}{=} \\ &\stackrel{2}{=} \tilde{u}(t, r, \theta, \varphi - \omega t - \omega\tau) \stackrel{3}{=} u(t, r, \theta, \varphi - \omega\tau). \end{aligned}$$

Identities 1 and 3 are due to the definition of  $\tilde{u}$ , while equality 2 is because  $\tilde{u}$  is a  $\tau$  periodic function.

Taking into account that  $\partial_t u = \partial_t \tilde{u} - \omega \partial_{\tilde{\varphi}} \tilde{u}$  and Eq. (7), the equations for  $\tilde{u}(t, r, \theta, \tilde{\varphi})$  are deduced. By omitting the tildes, they are

$$\partial_t u = L_0^{-1} (L(p)u + B(u, u)) + \omega \partial_\varphi u. \quad (10)$$

The periodic orbits of this system are MRW of Eq (7), and its fixed points correspond to RW of Eq (7).

#### Continuation of the MRW

To study the dependence of the MRW on the parameter  $p = Ra$ , pseudo-arclength continuation methods are used. They allow to obtain the curve of solutions  $x(s) = (u(s), \tau(s), \omega(s), p(s)) \in \mathbb{R}^{n+3}$ ,  $s$  being the arclength parameter, by adding the pseudo-arclength condition

$$m(u, \tau, \omega, p) \equiv \langle w, x - x^0 \rangle = 0, \quad (11)$$

$x^0 = (u^0, \tau^0, \omega^0, p^0)$  and  $w = (w_u, w_\tau, w_\omega, w_p)$  being the predicted point and the tangent to the curve of solutions, respectively, obtained by extrapolation of the previous points along the curve.

The system which determines a single solution,  $x = (u, \tau, \omega, p)$  is

$$H(u, \tau, \omega, p) = \begin{pmatrix} u - \phi(\tau, u, \omega, p) \\ g(u) \\ h(u) \\ m(u, \tau, \omega, p) \end{pmatrix} = 0, \quad (12)$$

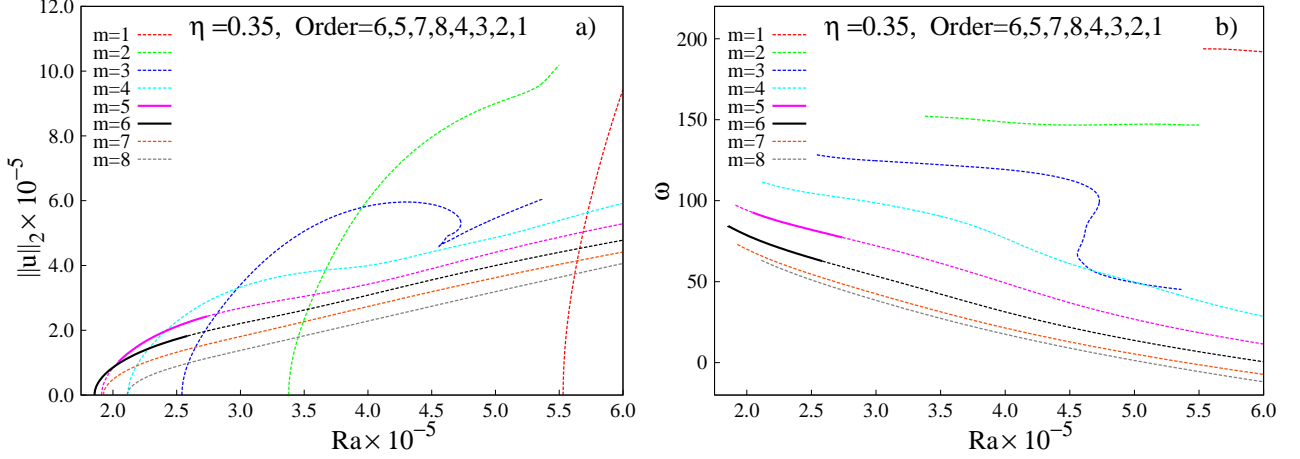


FIG. 1. Bifurcation diagram (taken from [31]) showing (a) the  $\mathcal{L}_2$ -norm of the RW and (b) the drifting frequency,  $\omega$ , both versus  $Ra$ .

where  $\phi(\tau, u, \omega, p)$  is solution of Eq. (10) at time  $t = \tau$  with initial condition  $u$  at  $t = 0$ , and for fixed  $\omega$  and  $p$ . The conditions  $g(u) = 0$  and  $h(u) = 0$  are selected to fix the two undetermined phases of the MRW. We use  $g(u) = \langle u, \partial_\varphi u_c \rangle = 0$  and  $h(u) = \langle u, \partial_\varphi^3 u_c \rangle = 0$ , where  $u_c$  is a reference solution (the eigenvector,  $u_c = v_c$ , at  $p = p_2$ , a previously computed solution, or the extrapolated value of  $u$  at the first iteration). The former is a necessary condition for  $\|u - u_c\|_2^2$  to be minimal with respect to the phase (see [31]), and the latter is selected to ensure  $h(u_c) = 0$ . For the computation of the inner products  $\langle \cdot, \cdot \rangle$  between two functions expanded in spherical harmonics we use the definitions of [31].

To solve the large non-linear system defined by Eq. (12) we use Newton-Krylov methods. They are matrix-free methods that do not require the explicit computation of the jacobian  $D_{(u,\tau,\omega,p)}H(u, \tau, \omega, p)$ , but only its action on a given vector. For the linear systems we use GMRES [30]. Due to the particular form of the spectrum of  $D_{(u,\tau,\omega,p)}H(u, \tau, \omega, p)$  for dissipative systems, GMRES does not need preconditioning (see [34] for details).

The action of the Jacobian  $D_{(u,\tau,\omega,p)}H(u, \tau, \omega, p)$  on  $\delta x = (\delta u, \delta \tau, \delta \omega, \delta p) \in \mathbb{R}^{n+3}$  is

$$\begin{pmatrix} \delta u - v(\tau) - \dot{z}(\tau)\delta\tau \\ D_u g(u)\delta u \\ D_u h(u)\delta u \\ D_x m(x)\delta x \end{pmatrix} \in \mathbb{R}^{n+3}. \quad (13)$$

Here  $z(\tau), v(\tau) \in \mathbb{R}^n$  are the solutions, at time  $t = \tau$ , of the system

$$\partial_t z = L_0^{-1}(L(p)z + B(z, z)) + \omega \partial_\varphi z, \quad (14)$$

$$\begin{aligned} \partial_t v &= L_0^{-1}(L(p)v + B(z, v) + B(v, z)) + \\ &+ \omega \partial_\varphi v + \delta \omega \partial_\varphi z + \delta p L_0^{-1} L^{(2)} z, \end{aligned} \quad (15)$$

with initial conditions  $z(0) = u$  and  $v(0) = \delta u$ , with fixed  $\omega$  and  $p$ . The dependence of  $L$  on  $p$ , of the form  $L(p) = L^{(1)} + pL^{(2)}$  has been used. Each GMRES iteration will require one evaluation of the jacobian, therefore

most of the computational cost is consumed in the integration over one tentative modulation period of a large ODE system of dimension  $2n$ . Thus, an efficient time integration is mandatory.

Notice that the RW can be obtained with the code written to compute MRW by omitting the term  $\omega \partial_\varphi u$  in Eq. (10), and the dependence of  $\omega$  and the phase condition  $h(u)$  of Eq. (12). In this case  $\tau$  means the period of the RW. However, the time integration can be reduced by a factor  $m$  due to their  $m$ -fold spatial symmetries. Moreover, since the fixed points of system (10) are RW of system (7), they can also be computed with the same code by removing the dependence on  $\tau$  and one phase condition in Eq. (12). Now the flying time  $\tau$  appearing in the first component of Eq. (12) is no longer an unknown but a fixed characteristic time. It should be small to avoid long time integrations but large enough to have a fast convergence of the linear solver. We have used these tricks to check the new code for the computation of MRW by comparing with previous results. These calculations are more demanding than those used in [31] because they involve time integrations of  $2n$  equations, but they are easier to implement, if a time-stepper code is available, because GMRES does not need preconditioning in contrast to what happened in [31].

### Stability of the MRW

Suppose a MRW  $(u, \tau, \omega, p) \in \mathbb{R}^{n+3}$  has been found. To study the stability of this periodic solution, Floquet theory is applied. Handling the full Jacobian matrix  $D_u \phi(\tau, u, \omega, p)$ ,  $\phi(\tau, u, \omega, p)$  being the solution of Eq. (10) at time  $t = \tau$  with initial condition  $u$  at  $t = 0$  and for fixed  $\omega$  and  $p$ , would require a prohibitive amount of memory due the high resolutions employed in the present study. It is enough to compute the leading eigenvalues and eigenvectors of the map  $\delta u \rightarrow D_u \phi(\tau, u, \omega, p)\delta u = v(\tau)$ ,  $v(\tau)$  being the solution of the first variational equa-

tion obtained by integrating the system

$$\begin{aligned}\partial_t z &= L_0^{-1}(L(p)z + B(z, z)) + \omega \partial_\varphi z, \\ \partial_t v &= L_0^{-1}(L(p)v + B(z, v) + B(v, z)) + \omega \partial_\varphi v\end{aligned}$$

of dimension  $2n$ , with initial conditions  $z(0) = u$  and  $v(0) = \delta u$ , over a modulation period  $\tau$ , with fixed  $\omega$  and  $p$ .

The leading eigenvalues of the map, which correspond to the leading Floquet multipliers, are computed by using the ARPACK package. MRW with leading Floquet multipliers with modulus larger (smaller) than  $+1$  are unstable (stable). Notice that in this problem, for any value of  $p$ , there are two marginal ( $+1$ ) Floquet multipliers due to the invariance under azimuthal rotations and time translations, with associated eigenfunctions  $v_1 = \partial_t u$  and  $v_2 = \partial_\varphi u$ . To avoid unnecessary computations they can be deflated by computing the eigenvalues of the map  $\delta u \rightarrow v(\tau) - \langle v(\tau), v_1 \rangle v_1 - \langle v(\tau), v_2 \rangle v_2$ . This method to determine the stability of the solutions is very robust but computationally expensive because it requires the time integration of an ODE system of dimension  $2n$  over one period of the modulation. Since the solution is a periodic orbit of Eq. (10) there is no cheaper alternative to this procedure.

## V. RESULTS

### A. Branches of modulated waves

The eigenfunctions at the bifurcation points of Fig. 1 were used to identify the azimuthal symmetries of the MRW and in this way to build initial conditions to start their continuation. The modulation periods  $\tau_i^m = 2\pi / \text{Im}(\lambda_i^m)$  of the branches of MRW at the critical parameters  $p_i^m$  are obtained from the leading eigenvalues,  $\lambda_i^m$ , at the Hopf bifurcations. The initial drifting frequencies  $\omega_i^m$  are those of the RW,  $(u_i^m, \omega_i^m, p_i^m)$ , at the bifurcation points. All the results shown in this section (otherwise mentioned) are obtained with truncation parameters  $n_r = 32$  and  $L_{max} = 60$ .

Figure 2(a) and their blowups in Figs. 2(b,c,d) display the drifting frequency,  $\omega$ , versus  $Ra$  for the RW with five- or six-fold rotational symmetry (in red) and for the MRW without any azimuthal symmetry ( $m = 1$  MRW from now on) and those with five- or six-fold rotational symmetries (in blue). The meaning of dashes and symbols can be seen in the figure caption. While for the RW the frequency  $\omega$  always decreases monotonically, for the five- or six-fold symmetric MRW it increases at the beginning of the branch but starts to decrease soon. In contrast, the behavior of  $m = 1$  MRW is more complex. On average,  $\omega$  decreases, but it increases in the regions where saddle-node bifurcations are present (see Figs. 2(b) and 2(d)).

As said before, the unstable  $m = 1$  branch of MRW arises from the five-fold symmetric branch of RW (see

fig. 2(b)). At a saddle-node bifurcation at  $Ra_1^1 = 2.15713 \times 10^5$  it becomes stable down to  $Ra_2^1 = 2.15690 \times 10^5$ , where a Hopf bifurcation occurs. This interval of stability is very small, as shows the detail of Fig. 2(b), so it would be nearly impossible to capture it with direct simulations. The stability analysis of the solutions along this branch has allowed to identify several bifurcations. The detail of most of the saddle points is shown in fig. 2(d). Notice that in the latter figure some of the bifurcations are very close, therefore if a second parameter is varied (for instance  $E$  or  $\sigma$ ) codimension two bifurcations (Hopf–saddle-node, double-Hopf, period-doubling–saddle-node) could be located. Finally, the branch of  $m = 1$  MRW ends at a Hopf bifurcation again on the five-fold symmetric branch of RW (see right-bottom corner of fig. 2(d)).

In contrast to the  $m = 1$  branch of MRW, the regions of stability of the 6, 5-fold MRW are sufficiently large (see Fig. 2(c)) as to capture these solutions by time integration [8]. We have identified the bifurcations on these branches and checked that the MRW starting at the first period-doubling bifurcation found correspond to the solutions computed in [11] by using azimuthal-symmetry-constrained time integration. In the latter work, in agreement with Feigenbaum’s theory, up to three period-doublings leading to chaotic solutions were found.

The bifurcation diagrams of the time-averaged Nusselt number,  $\overline{Nu}$  and kinetic energy density,  $\overline{K}$ , both defined as in [13], are shown in Fig. 2(e) and Fig. 2(f), respectively. The curves of RW are very smooth and  $\overline{Nu}$  and  $\overline{K}$  increase monotonically with increasing  $Ra$ . In contrast, the curves of MRW are not monotonous and the  $m = 1$  branch has a marked loop. Note that at  $Ra = 4.1 \times 10^5$  there are five unstable solutions without azimuthal symmetries and very different values of  $\overline{Nu}$  and  $\overline{K}$ . The  $m = 1$  branch of MRW has the larger  $\overline{Nu}$ , with the maximum very near from a Hopf–saddle-node bifurcation (the saddle-node at  $Ra_{12}^1 = 4.43366 \times 10^5$  and the Hopf point at  $Ra_{11}^1 = 4.43358 \times 10^5$ ). This solution has also large values of  $\overline{K}$  comparable to those of the five-fold symmetric MRW around  $Ra = 5.8 \times 10^5$ .

In Fig. 3(a) the modulation period  $\tau$  for the three branches of MRW shown in Fig. 2 is plotted versus  $Ra$ , with a detail in Fig. 3(b) of the double-loop where the  $m = 1$  branch undergoes several bifurcations. Each branch of Fig. 3(a) starts with a modulation period  $\tau$  given by the stability analysis of the RW at the corresponding bifurcation point. It is worth noticing that the theoretically predicted  $\tau$  could not be minimal in the sense that there might exist another modulation period  $\tau' = \tau/k$  with  $k \in \mathbb{N}$ , and another drifting frequency  $\omega' = \omega - 2\pi/\tau$  such that  $(u, \tau', \omega', p)$  is also a MRW (see [29]). For the five- or six-fold branches the modulation period  $\tau$  obtained from the stability analysis is minimal. However, for the  $m = 1$  MRW the minimal period is  $\tau' = \tau/5$ . Detecting  $\tau'$  is important to avoid unnecessary time integrations which are the most expensive

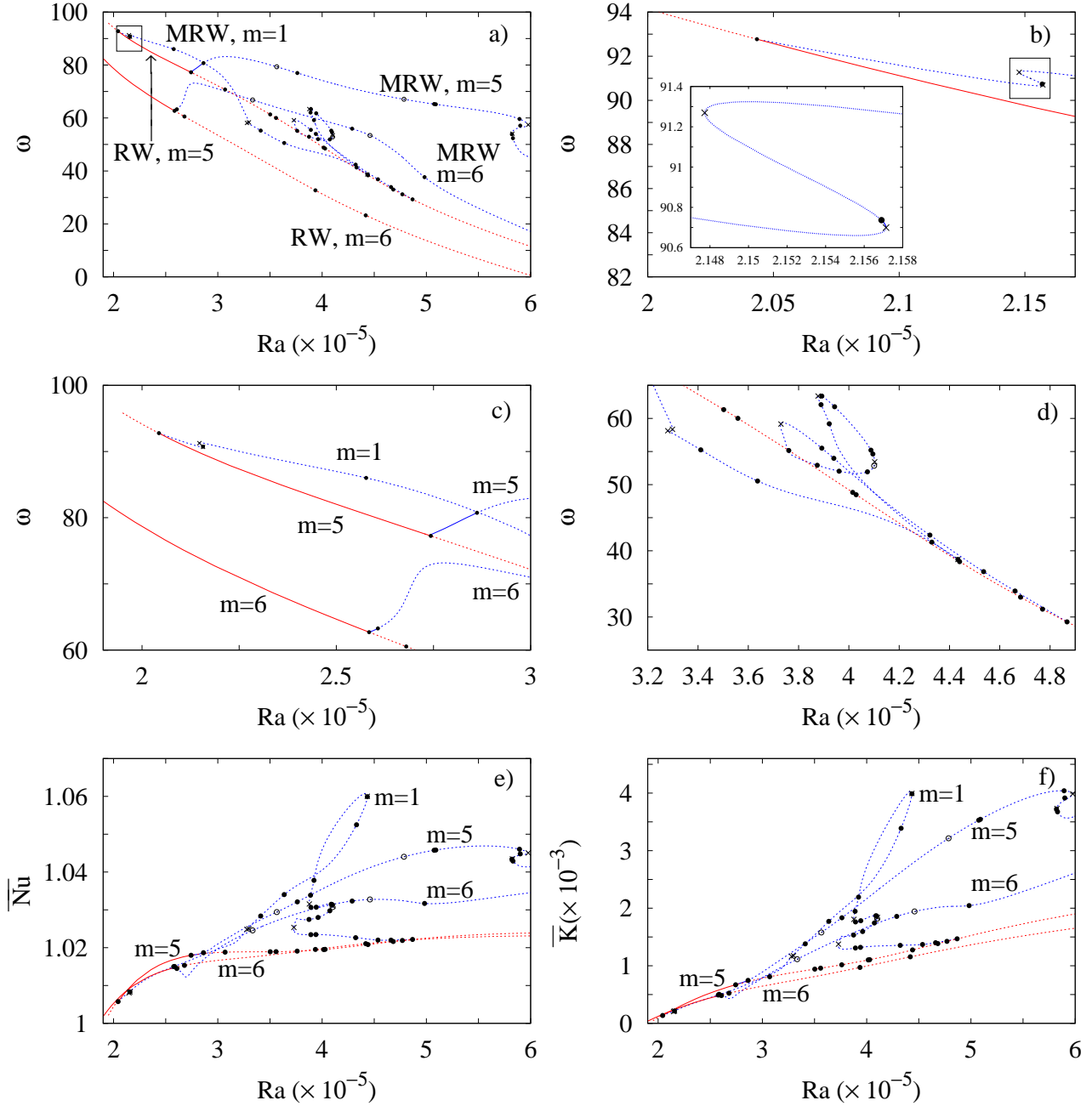


FIG. 2. Bifurcation diagrams: (a) Drifting frequency,  $\omega$ , versus  $Ra$ . (b) Detail corresponding to the square drawn in Fig. 2(a). (c) Detail containing the regions of stable RW and MRW. (d) Detail showing the loops on the  $m = 1$  branch of MRW and the five-fold branch of RW. (e) Time-averaged Nusselt number,  $\overline{Nu}$ , and (f) time-averaged kinetic energy density,  $\overline{K}$ , both versus  $Ra$ . Solid (dashed) lines indicate stable (unstable) solutions. The symbols mean the types of bifurcations: ( $\bullet$ ) Hopf, ( $\times$ ) saddle-node and ( $\circ$ ) period-doubling.

computational task. An algorithm to obtain  $\tau'$  and  $\omega'$  directly from an observable of an experiment with  $O(2)$  symmetry was presented in [27]. The modulation period is obtained from the period of the time series of a volume-averaged quantity. This also applies to our problem because volume-averaged quantities are invariant under azimuthal rotations.

Figure 4, showing the modulus of the two leading Floquet multipliers,  $|\mu_1| \geq |\mu_2|$ , plotted versus the Rayleigh number, helps to illustrate how the  $m = 1$  branch of MRW gains and loses stability in the double-fold of Fig. 2(b). The modulus of  $\mu_1$  is plotted in solid line and  $|\mu_2|$  in dashed line. The symbol  $\bullet$  signals the values of  $|\mu_1|$  and  $|\mu_2|$  at the starting point, and the arrows

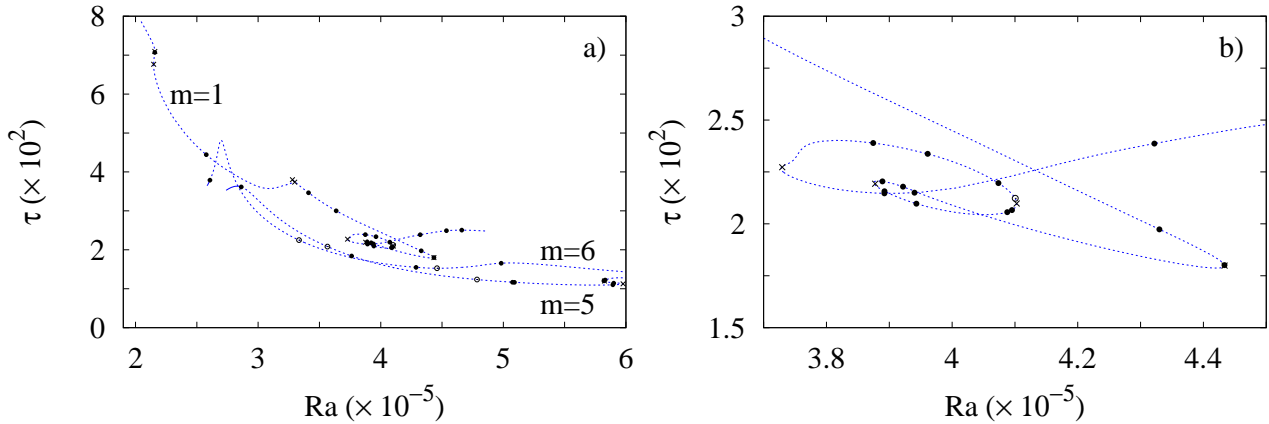


FIG. 3. (a) Bifurcation diagram of the modulation period,  $\tau$ , of the MRW versus  $Ra$ . (b) Detail showing the loop of the  $m = 1$  branch. The type of dash and symbols mean the same as in Fig. 2

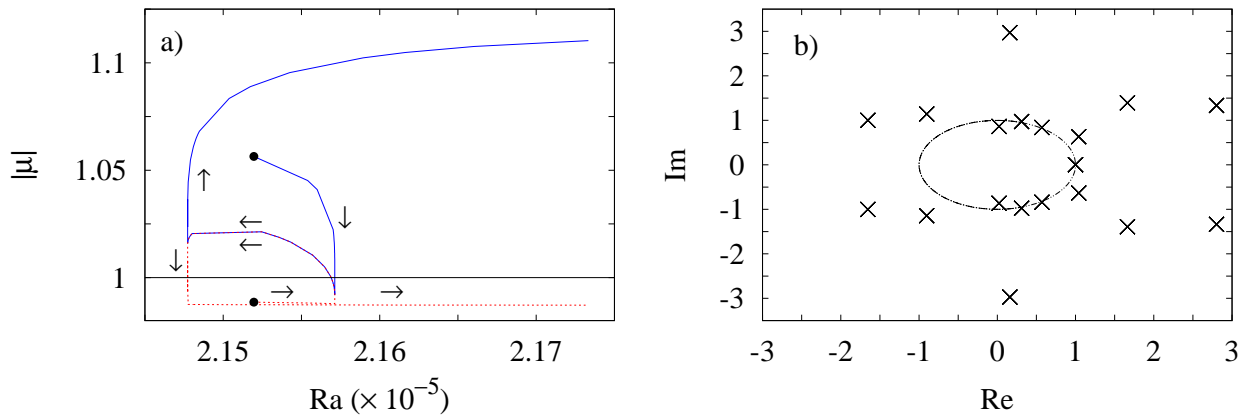


FIG. 4. (a) Modulus of the two leading Floquet multipliers versus  $Ra$ , for the solutions shown in the detail of Fig. 2(b). (b) Leading Floquet multipliers of the last solution calculated on the  $m = 1$  branch. The closed curve is the unit circle.

indicate the path followed along the curve. The crossings through the horizontal line placed at  $|\mu| = 1$  mark the three bifurcation points along the curve. At the beginning both multipliers are real. When the first crosses the unit circle it stabilizes the fluid at the first saddle-node bifurcation. Afterwards, it collapses with the second forming a complex conjugated pair of  $|\mu| < 1$  that crosses again the unit circle. This is the Hopf bifurcation that destabilizes the  $m = 1$  branch of MRW. Finally the pair separates after colliding on the real axis. The first real multiplier increases its modulus and the second crosses again the unit circle at the second saddle-node bifurcation.

Figure 4(b) displays the twenty first leading Floquet multipliers for the last solution computed on the  $m = 1$  branch of MRW, which ends again on the five-fold RW. There are nine complex conjugated pairs, eight of them

outside the unit circle, and two real, so close to each other, that are indistinguishable in the figure. One of them is outside the unit circle. This means that several of the bifurcations detected along this branch (as much as 29) are due to multipliers entering to the unit circle. Except in the three Hopf bifurcations where the stable MRW lose their stability, any other Hopf or period-doubling bifurcations gives rise to unstable three-frequency solutions or period-doubled MRW, respectively. For instance, twenty branches of unstable objects are born along only the  $m = 1$  branch. Thus the phase space of this problem is so complex that it is almost impossible to unfold a small part of the full bifurcation diagram. However in some cases, as in [31], chaotic finite-amplitude solutions at this range of parameters can be understood as trajectories which visit in a random way the stable RW and MRW, pointing out the

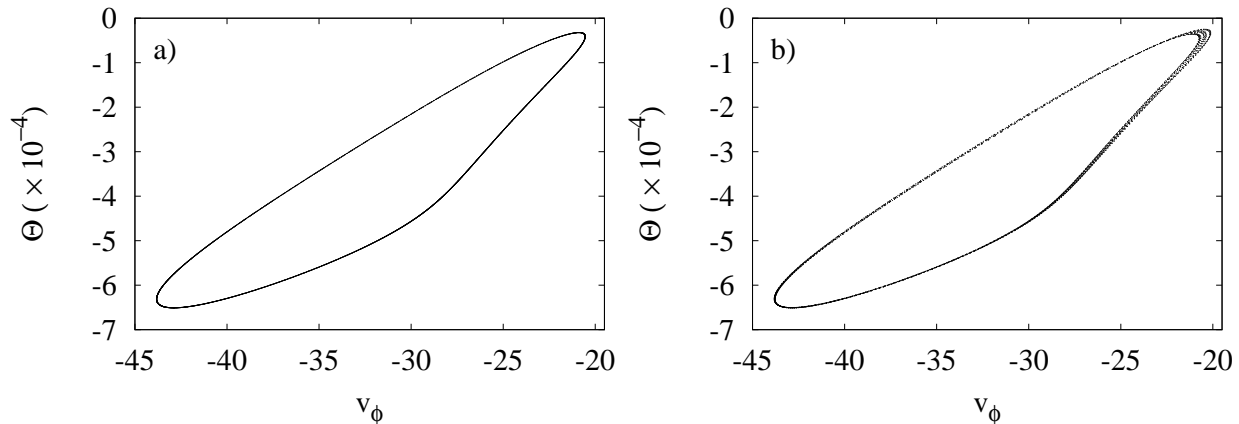


FIG. 5. Poincaré section at  $\Theta((r_o+r_i)/2, 0, 3\pi/8) = 0$  of the azimuthal component of the velocity field  $v_\varphi(r_i+(r_o-r_i)/7, 0, 3\pi/8)$  plotted versus  $\Theta$  at the same point. (a) Stable  $m = 1$  MRW at  $Ra = 2.15701 \times 10^5$ . (b) Stable three-tori bifurcated from the  $m = 1$  MRW at  $Ra = 2.15685 \times 10^5$ .

interest of the computation of unstable solutions by continuation methods.

When the MRW lose their stability via Hopf bifurcations, branches of three-frequency solutions (three-tori) of Eq. (7) or two-frequency RW (two-tori) of Eq. (10) arise at the bifurcation points. By means of time integration of Eq. (7), the three stable three-tori bifurcated from the five- or six-fold MRW and the  $m = 1$  MRW have been found. The Poincaré section at  $\Theta((r_o + r_i)/2, 0, 3\pi/8) = 0$  of the azimuthal component of the velocity field  $v_\varphi(r_i + (r_o - r_i)/7, 0, 3\pi/8)$  plotted versus  $\Theta$  at the same point, for a stable  $m = 1$  MRW at  $Ra = 2.15701 \times 10^5$ , is displayed in Fig. 5(a). Figure 5(b) shows the same Poincaré section but for the stable three-tori at  $Ra = 2.15685 \times 10^5$ , bifurcated from the  $m = 1$  MRW. In this case the section is no longer a curve but a band. It is worth to notice that both type of oscillatory solutions are obtained from initial conditions given by the continuation code. Although they are stable near  $Ra_c$ , their stability interval is very short, and the basin of attraction of the stable five- or six-fold symmetric RW is much larger than that of the  $m = 1$  MRW and three-tori of Eq. (7), then it would be almost impossible to get them by chance with time integrations.

The flow patterns along the  $m = 1$  branch of MRW are shown in Fig. 6. It shows, from top to bottom, a sequence of solutions at  $Ra = 2.04612 \times 10^5, 2.20259 \times 10^5, 3.23559 \times 10^5, 4.31323 \times 10^5, 4.87302 \times 10^5$ . Three projections of the temperature perturbation are displayed in the left group of plots. The radius of the spherical surfaces ranges from  $r = r_i + 0.22d$  to  $r = r_i + 0.3d$ , although they are represented with the same size as the other sections. They correspond approximately to the location where the columns of  $\Theta$  get the maximum. The middle projections are taken on the equatorial plane, and the right ones on a meridional section that cuts the equatorial cell of  $\Theta$  by its maximum. The scale of colors is the

same in each solution, with blue meaning cold fluid. The same projections are taken for the kinetic energy density  $K$  (right group of plots), but with the spherical projections taken close to the outer boundary at  $r = r_i + 0.975d$ , where it reaches its maximum at high latitudes, and with the spherical surface seen from the pole.

The meridional sections show the typical patterns of convection in a regime where rotation plays a dominant role in the dynamics: the  $z$ -dependence of the flow is weak, and outside a columnar region the fluid is nearly stagnant. The cells of convection are symmetric with respect to the equatorial plane and attached to the inner sphere. The equatorial sections of  $K$  display a double-layered pattern of spiraling vortices. The solutions close to the five-fold RW have the symmetry weakly broken and the five convective cells have similar size (see first and last rows of Fig. 6). In contrast, far away the bifurcation points, the number of convective cells diminishes, some of them are significantly smaller than the others and the convection is localized in patches whose intensity grows and decays while the full pattern is rotating.

Contour plots along the five-fold branch of MRW at  $Ra = 2.73868 \times 10^5, 3.32581 \times 10^5, 4.00390 \times 10^5, 5.22800 \times 10^5, 5.82313 \times 10^5$  are shown in Fig. 7. The patterns of the first solution resemble those of the five-fold RW at the bifurcation point. As the Rayleigh number is increased, the cells of hot fluid spiral and expand to the outer boundary, confining the cold fluid in small cells near the interior. In addition, the vortices of  $K$  become connected near the inner boundary indicating that there are strong internal mean zonal circulations in this region of parameters (see for instance the third row at  $Ra = 4.00390 \times 10^5$ ). The same behavior was found when the six-fold MRW were analyzed.

Figure 8, 9 and 10 display, respectively, the contour plots of  $\Theta$  and  $K$  for the  $m = 1$  MRW, the five- or six-fold MRW at the Hopf bifurcation points where they lose

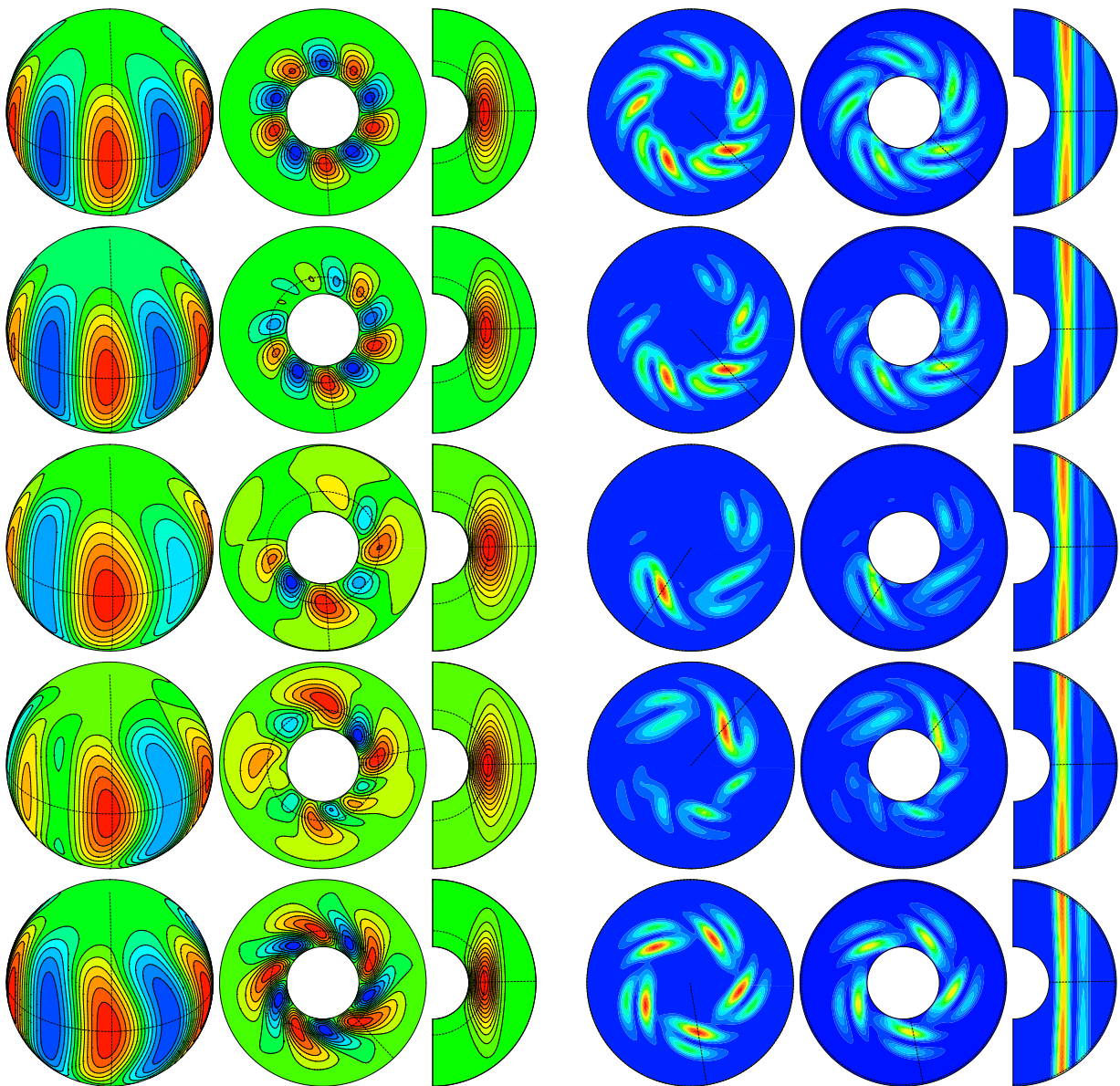


FIG. 6. The left column of three plots contains the contour plots of  $\Theta$  on a sphere, on the equatorial plane, and on a meridional section, for solutions lying on the  $m = 1$  branch of MRW at  $Ra = 2.04612 \times 10^5, 2.20259 \times 10^5, 3.23559 \times 10^5, 4.31323 \times 10^5, 4.87302 \times 10^5$  (from top to bottom). The right column corresponds to  $K$  for the solution and same  $Ra$ .

stability, and the corresponding real and imaginary parts of the critical eigenfunction. At the bifurcation the symmetry of the five- or six-fold MRW is broken, but as can be seen in the second and third rows of Fig. 10 the eigenfunction of the six-fold MRW is invariant under a rotation of  $\pi$ . Therefore the three-frequency of waves emerging at this point retains a two-fold rotational symmetry.

Finally, to check the sensibility of the bifurcation points with the spatial resolution, the variation of  $Ra$ ,  $\tau$ ,  $\omega$  and the argument of the leading eigenvalue,  $\text{Arg}(\lambda)$ , is studied for the four bifurcations where the MRW become stable or unstable. The results are included in table I. We have changed both, the number of radial collocation points,  $n_r$ , and the spherical harmonics truncation

parameter,  $L_{max}$ . The computation of the five- or six-fold symmetric branches is performed applying symmetry constraints to reduce the size of the systems,  $n$ , required to obtain them. In contrast, all the modes must be retained when computing the branch without rotational symmetry. The values of  $n$  range from 57692 up to 1061977. When analyzing the stability of the solutions no symmetry constraints are imposed. In this case the number of discretization points range from 345991 up to 1061977. The determination of the critical point was performed in each case by inverse interpolation.

As can be seen in the table the accuracy of the results is very good. Even with the lower resolutions used at least three significant figures are obtained for  $\text{Arg}(\lambda)$  and four

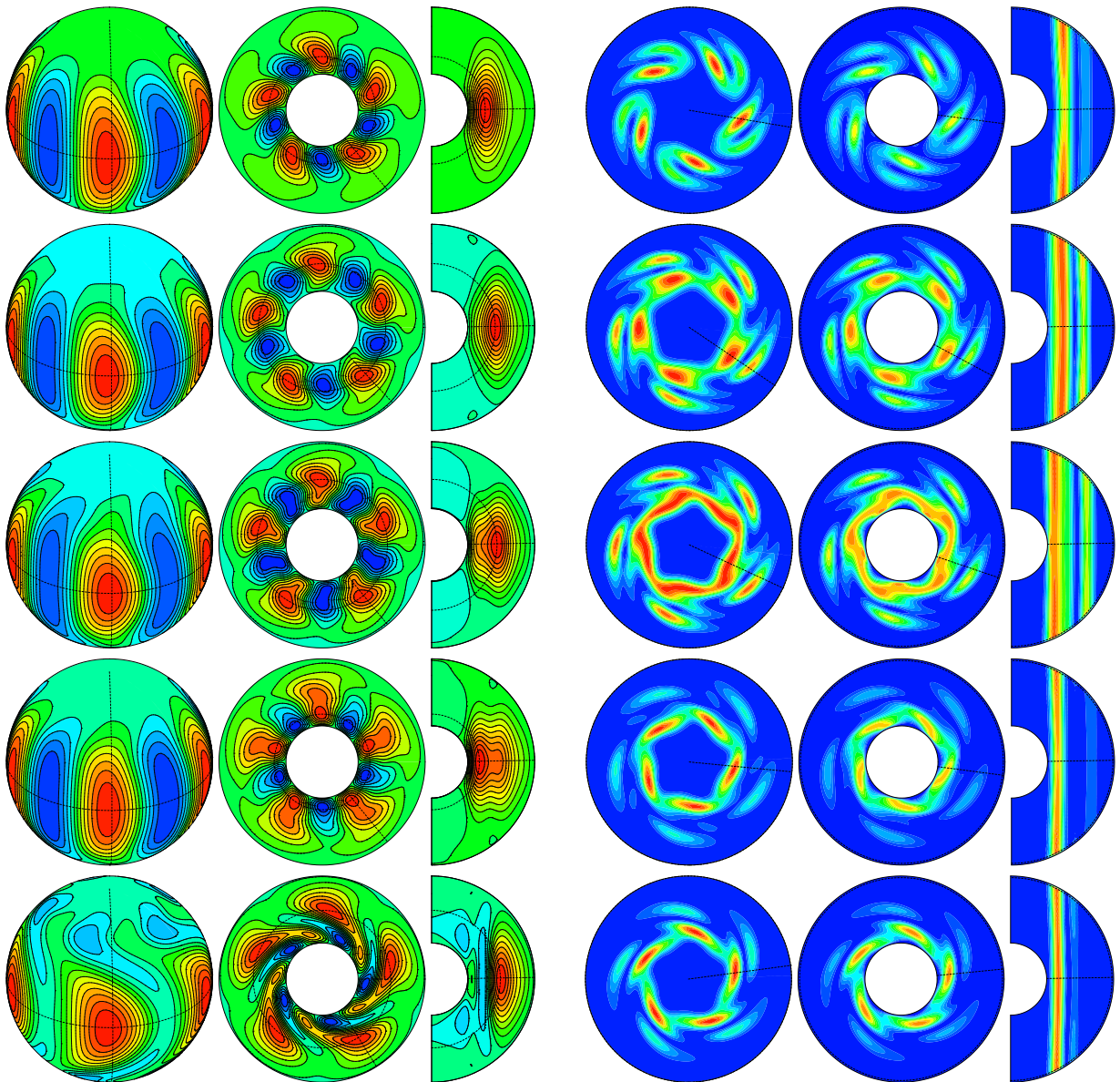


FIG. 7. Same contour plots as in Fig. 6 for five-fold symmetric solutions at  $Ra = 2.73868 \times 10^5, 3.32581 \times 10^5, 4.00390 \times 10^5, 5.22800 \times 10^5, 5.82313 \times 10^5$  (from top to bottom).

or more for the other quantities.

## VI. SUMMARY

Modulated thermal Rossby waves and their stability have been computed in rotating spherical geometry for parameter values of  $\sigma$  and  $\eta$  of geophysical relevance.

The MRW have been obtained as periodic orbits in the rotating frame of reference where only the period of the modulation is observed. Newton-Krylov continuation allows to obtain unstable RW and MRW that cannot be found by only using time integrations. The use matrix-free linear solvers for the Newton iterations avoid the storage of the Jacobian matrix allowing to tackle high

resolutions needed for low Ekman and Prandtl number flows. In this way we have been able to compute stable MRW stabilized at a saddle-node bifurcation of an unstable branch of MRW.

To find a single MRW up to relative tolerance  $10^{-8}$  the Newton-Krylov method typically converges in 4 Newton iterations. Each of them requires an evaluation of the function, i.e, one time integration of an ODE system of dimension  $n = O(10^5 - 10^6)$  plus an average of 15 GMRES iterations, i.e, 15 additional time integrations of an ODE system of dimension  $2n$  are needed. Close to the bifurcation points the convergence slows down, so efficient and accurate (high-order) time integration is essential.

We have performed an exhaustive stability analysis to detect and classify the large sequence of bifurcations that

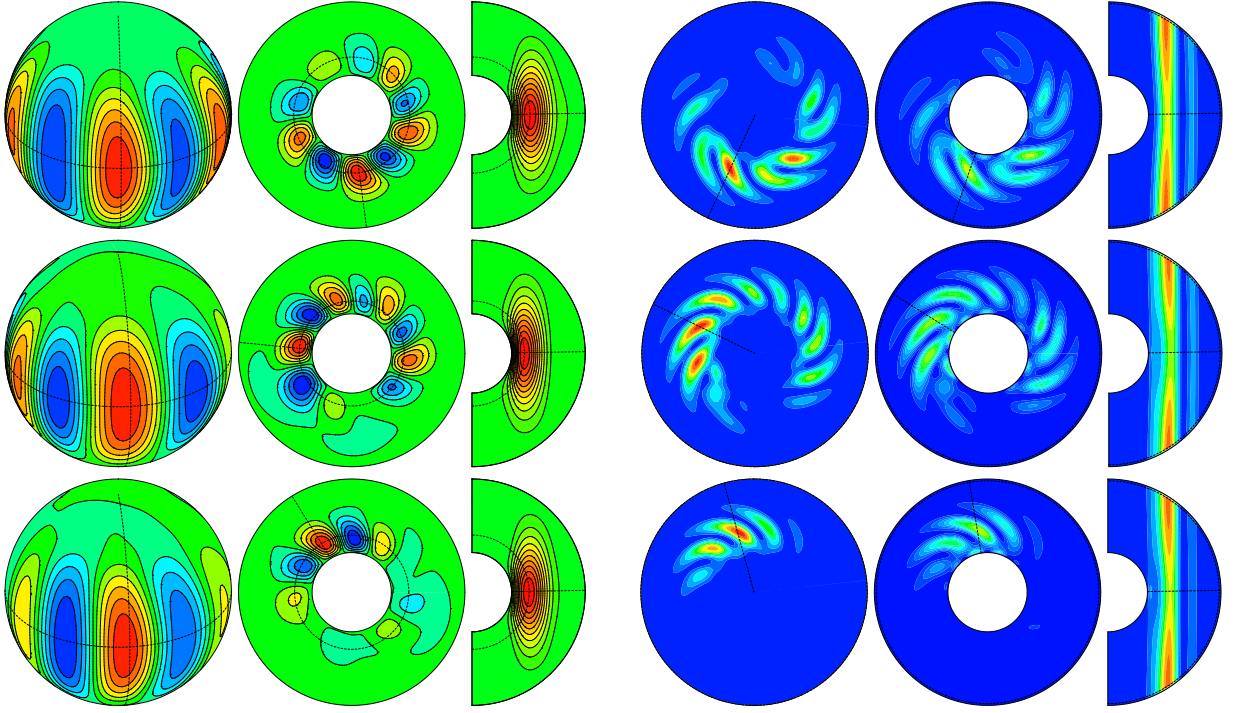


FIG. 8. Same type of contour plots as in Fig. 6. The first row corresponds to  $\Theta$  and  $K$  for the solution at the first Hopf bifurcation point ( $Ra_2^1 = 2.15690 \times 10^5$ ) on the  $m = 1$  branch, the next two rows show the real and imaginary parts of the leading eigenfunction at the same point.

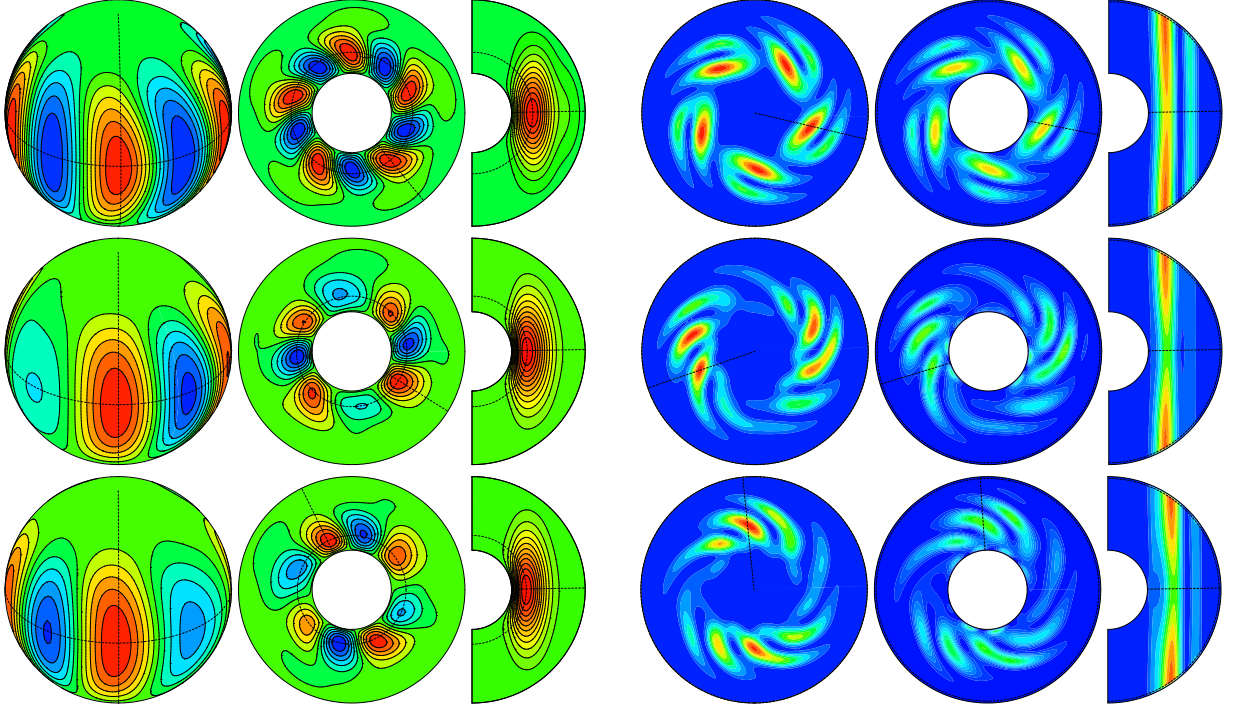


FIG. 9. Same contour plots as in Fig. 8 for the solution and the real and imaginary parts of the leading eigenfunction at the first Hopf bifurcation point ( $Ra_1^5 = 2.86197 \times 10^5$ ) on the five-fold branch.

takes place along these branches. In contrast to what happens with the RW, we have found that the range of  $Ra$  in which the MRW are stable is very small. This

is specially true in the case of the  $m = 1$  MRW, stable very close to the onset at  $Ra/Ra_c = 1.16$ . The stability regions of the RW and MRW overlap giving rise to regions

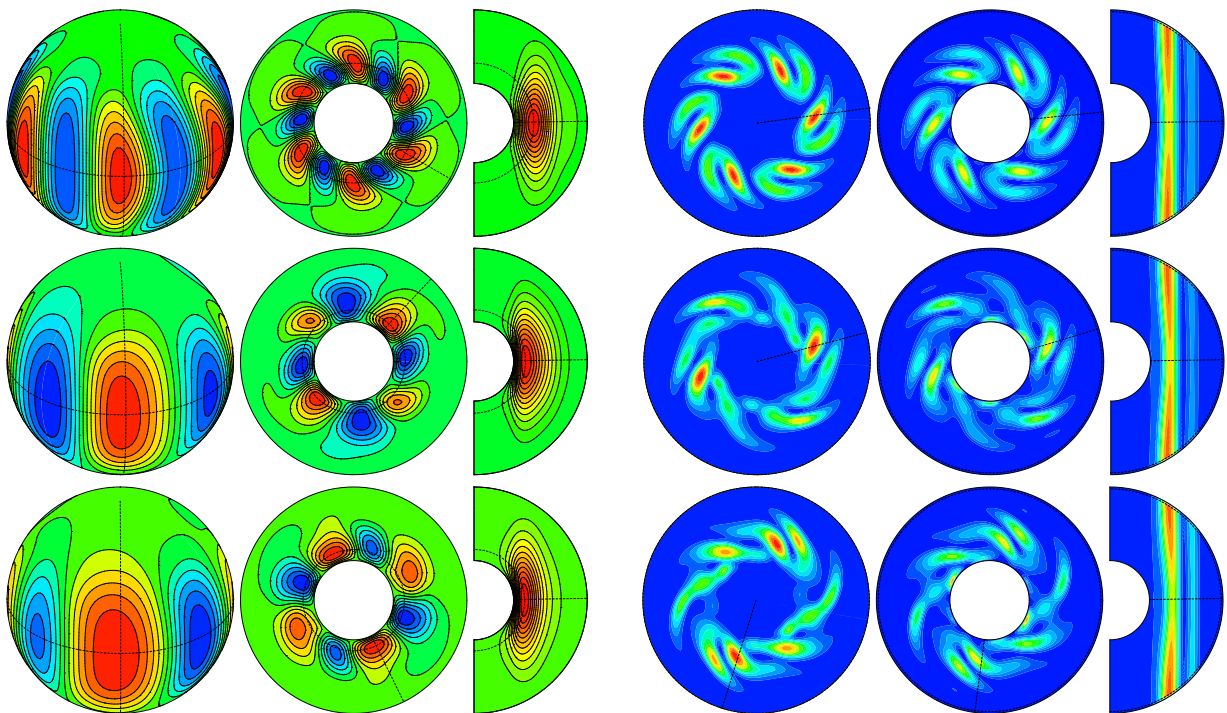


FIG. 10. Same contour plots as in Fig. 9 for the solution and the real and imaginary parts of the leading eigenfunction at the first Hopf bifurcation point ( $Ra_1^6 = 2.60701 \times 10^5$ ) on the six-fold branch.

$n_r$	$m$	$\frac{L_{max}}{m}$	$n$	$R_c$	$\tau$	$\omega$	$\text{Arg}(\lambda)$
32	1	60	345991	215713.2	0.0709448	90.6995	0
40	1	72	623415	215716.7	0.0709454	90.6989	0
50	1	84	1061977	215716.7	0.0709454	90.6989	0
32	1	60	345991	215689.7	0.0706949	90.7367	0.0388974
40	1	72	623415	215692.4	0.0706954	90.7363	0.0389272
50	1	84	1061977	215692.4	0.0706953	90.7363	0.0389286
32	5	12	69223	286197.3	0.0361569	80.7386	2.47680
40	5	14	117975	286203.6	0.0361561	80.7383	2.47700
50	5	16	192913	286203.8	0.0361561	80.7384	2.47701
32	6	10	57691	260700.8	0.0378892	63.2709	1.13710
40	6	12	103935	260703.5	0.0378885	63.2706	1.13703
50	6	14	177037	260703.4	0.0378885	63.2706	1.13704

TABLE I. Variation of the critical parameters of the MRW at the Hopf bifurcations where they change the stability with the resolution.

of multistability of two and three different types of waves.

The five- or six-fold and  $m = 1$  MRW lose their stability via tertiary Hopf bifurcations, giving rise to three-frequency stable solutions. In addition, we have found more than 50 Hopf and period-doubling bifurcations along the branches of RW and MRW studied. These bifurcations give rise to branches of unstable modulated and three-frequency waves which configure the skeleton of the phase space. To have the tools to compute them is important because the study of the unstable branches of solutions could explain the origin of stable temporally-chaotic flows observed experimentally in the same range of parameters or computed from uncontrolled initial conditions.

## VII. ACKNOWLEDGMENTS

This research has been supported by MEC-DGICT/FEDER project FIS2013-40674-P and AGAUR-GENCAT project 2014-SGR-1145.

- 
- [1] M. Ardes, F. H. Busse, and J. Wicht. Thermal convection in rotating spherical shells. *Phys. Earth Planet. Inter.*, 99:55–67, 1997.
- [2] U.R. Christensen. Zonal flow driven by strongly supercritical convection in rotating spherical shells. *J. Fluid*

- Mech.*, 470:115–133, 2002.
- [3] P. A. Davidson. Scaling laws for planetary dynamos. *Geophys. J. Inter.*, 195:67–74, 2013.
- [4] H. A. Dijkstra, F. W. Wubs, A. K. Cliffe, E. Doedel, I. F. Dragomirescu, B. Eckhardt, A. Y. Gelfat, A. L. Hazel,

- V. Lucarini, A. G. Salinger, E. T. Phipps, J. Sánchez-Umbria, H. Schuttelaars, L. S. Tuckerman, and U. Thiele. Numerical bifurcation methods and their application to fluid dynamics: Analysis beyond simulation. *Commun. Comput. Phys.*, 15(1):1–45, 2014.
- [5] C. Egbers, W. Beyer, A. Bonhage, R. Hollerbach, and P. Beltrame. The GEOFLOW experiment on ISS: I. Experimental preparation and design of laboratory testing hardware. *Adv. in Space Res.*, 32:171–180, 2003.
- [6] F. Feudel, N. Seehafer, L. S. Tuckerman, and M. Gellert. Multistability in rotating spherical shell convection. *Phys. Rev. E*, 87:023021–1–023021–8, 2013.
- [7] Matteo Frigo and Steven G. Johnson. The design and implementation of FFTW3. *Proceedings of the IEEE*, 93(2):216–231, 2005. special issue on "Program Generation, Optimization, and Platform Adaptation".
- [8] F. Garcia. *Thermal convection in rotating spherical shells*. Ph.D. thesis, Universitat Politcnica de Catalunya, 2012.
- [9] F. Garcia, E. Dormy, J. Sánchez, and M. Net. Two computational approaches for the simulation of fluid problems in rotating spherical shells. In G. R. Liu and Z. W. Guan editors, editors, *Proc. of the 5th International Conference on Computational Methods - ICCM2014. Cambridge, England*, volume 1, 2014.
- [10] F. Garcia, M. Net, B. García-Archilla, and J. Sánchez. A comparison of high-order time integrators for thermal convection in rotating spherical shells. *J. Comput. Phys.*, 229:7997–8010, 2010.
- [11] F. Garcia, J. Sánchez, E. Dormy, and M. Net. Oscillatory convection in rotating spherical shells: Low Prandtl number and non-slip boundary conditions. *SIAM J. Applied Dynamical Systems*, 2015.
- [12] F. Garcia, J. Sánchez, and M. Net. Antisymmetric polar modes of thermal convection in rotating spherical fluid shells at high Taylor numbers. *Phys. Rev. Lett.*, 101:194501–(1–4), 2008.
- [13] F. Garcia, J. Sánchez, and M. Net. Numerical simulations of thermal convection in rotating spherical shells under laboratory conditions. *Phys. Earth Planet. Inter.*, 230:28–44, 2014.
- [14] M. Golubitsky, V. G. LeBlanc, and I. Melbourne. Hopf bifurcation from rotating waves and patterns in physical space. *J. Nonlinear Sci.*, 10:69–101, 2000.
- [15] Kazushige Goto and Robert A. van de Geijn. Anatomy of high-performance matrix multiplication. *ACM Trans. Math. Softw.*, 34(3):1–25, 2008.
- [16] C. A. Jones. Thermal and compositional convection in the outer core. *Treat. Geophys.*, 8:131–185, 2007.
- [17] C. A. Jones, A. M. Soward, and A. I. Mussa. The onset of thermal convection in a rapidly rotating sphere. *J. Fluid Mech.*, 405:157–179, 2000.
- [18] G. Kawahara, M. Uhlmann, and L. van Veen. The significance of simple invariant solutions in turbulent flows. *Arch. Ration. Mech. An.*, 44:203–225, 2012.
- [19] H. B. Keller. Numerical solution of bifurcation and nonlinear eigenvalue problems. In P. H. Rabinowitz, editor, *Applications of Bifurcation Theory*, pages 359–384. Academic Press, 1977.
- [20] E.-J. Kim, D. W. Hughes, and A. M. Soward. A nonlinear dynamo driven by rapidly rotating convection. *Geophysical and Astrophysical Fluid Dynamics*, 98:325–343, April 2004.
- [21] K. Kimura, S. Takehiro, and M Yamada. Stability and bifurcation diagram of boussinesq thermal convection in a moderately rotating spherical shell. *Phys. Fluids*, 23:074101–1–074101–11, 2011.
- [22] R. B. Lehoucq, D. C. Sorensen, and C. Yang. *ARPACK User's Guide: Solution of Large-Scale Eigenvalue Problems with Implicitly Restarted Arnoldi Methods*. SIAM, 1998.
- [23] P. W. Livermore, D. W. Hughes, and S. M. Tobias. The role of helicity and stretching in forced kinematic dynamos in a spherical shell. *Phys. Fluids*, 19(5):057101–057101–9, 2007.
- [24] K. Meerbergen and D. Roose. Matrix transformations for computing rightmost eigenvalues of large sparse non-symmetric eigenvalue problems. *IMA J. Num. Anal.*, 16(3):297–346, 1996.
- [25] M. Net and J. Sánchez. Continuation of bifurcations of periodic orbits for large-scale systems. *SIAM J. Applied Dynamical Systems*, 14(2):674–698, 2015.
- [26] P. Olson. Laboratory experiments on the dynamics of the core. *Phys. Earth Planet. Inter.*, 187:1–18, 2011.
- [27] A. Palacios. Identification of modulated rotating waves in pattern-forming systems with  $O(2)$  symmetry. *Discrete Cont. Dyn. B*, 2(1):129–147, 2002.
- [28] M. R. E. Proctor and C. A. Jones. The interaction of two spatially resonant patterns in thermal convection. *J. Fluid Mech.*, 188:301–, 1988.
- [29] D. Rand. Dynamics and symmetry. Predictions for modulated waves in rotating fluids. *Arch. Ration. Mech. An.*, 79(1):1–37, 1982.
- [30] Y. Saad and M. H. Schultz. GMRES: a generalized minimal residual algorithm for solving nonsymmetric linear systems. *SIAM J. Sci. Stat. Comput.*, 7:865–869, 1986.
- [31] J. Sánchez, F. Garcia, and M. Net. Computation of azimuthal waves and their stability in thermal convection in rotating spherical shells with application to the study of a double-Hopf bifurcation. *Phys. Rev. E*, 87:033014/1–11, 2013.
- [32] J. Sánchez and M. Net. On the multiple shooting continuation of periodic orbits by Newton-Krylov methods. *Int. J. Bifurcation and Chaos*, 20(1):1–19, 2010.
- [33] J. Sánchez and M. Net. A parallel algorithm for the computation of invariant tori in large-scale dissipative systems. *Physica D*, 252(0):22 – 33, 2013.
- [34] J. Sánchez, M. Net, B. García-Archilla, and C. Simó. Newton-Krylov continuation of periodic orbits for Navier-Stokes flows. *J. Comput. Phys.*, 201(1):13–33, 2004.
- [35] J. Sánchez, M. Net, and C. Simó. Computation of invariant tori by Newton-Krylov methods in large-scale dissipative systems. *Physica D*, 239:123–133, 2010.
- [36] R. Simitev and F. H. Busse. Patterns of convection in rotating spherical shells. *New J. Phys.*, 5:97.1–97.20, 2003.
- [37] A. Tilgner and F.H. Busse. Finite amplitude convection in rotating spherical fluid shells. *J. Fluid Mech.*, 332:359–376, 1997.
- [38] L. van Veen, G. Kawahara, and M. Atsushi. On matrix-free computation of 2D unstable manifolds. *SIAM J. Sci. Comput.*, 33(25), 2011.
- [39] D. Viswanath. Recurrent motions within plane Couette turbulence. *J. Fluid Mech.*, 580(2):339–358, 2007.
- [40] T. Watanabe, K. Toyabe, M. Iima, and Y. Nishiura. Time-periodic traveling solutions of localized convection cells and their collision in binary fluid mixture. In *APS*

*Division of Fluid Dynamics Meeting Abstracts*, page H7, November 2010.

- [41] I. C. Waugh, S. J. Illingworth, and M. P. Juniper. Matrix-free continuation of limit cycles for bifurcation analysis of large thermoacoustic systems. *J. Comput. Phys.*, 240:225–247, 2013.
- [42] I. C. Waugh, K. Kashinath, and M. P. Juniper. Matrix-free continuation of limit cycles and their bifurcations for a ducted premixed flame. *J. Fluid Mech.*, 759:1–27, 2014.
- [43] K. K. Zhang. Convection in a rapidly rotating spherical shell at infinite Prandtl number: transition to vacillating flows. *Phys. Earth Planet. Inter.*, 72:236–248, 1992.